NeuroImage 211 (2020) 116609

Contents lists available at ScienceDirect

NeuroImage

journal homepage: www.elsevier.com/locate/neuroimage

# Microstructural correlates of $^{23}$Na relaxation in human brain at 7 Tesla

Scott C. Kolbe [a,b,c,*], Warda Syeda [c,d], Yasmin Blunck [e], Rebecca Glarin [c], Meng Law [a,b], Leigh A. Johnston [c,e,1], Jon O. Cleary [c,f,1]

[a] Department of Neuroscience, Central Clinical School, Monash University, Australia
[b] Department of Radiology, Alfred Hospital, Australia
[c] Department of Medicine and Radiology, University of Melbourne, Australia
[d] Melbourne Neuropsychiatry Centre, University of Melbourne, Australia
[e] Department of Biomedical Engineering, University of Melbourne, Australia
[f] Department of Radiology, Guy's and St. Thomas' NHS Foundation Trust, London, UK

ARTICLE INFO

*Keywords:*
Sodium MRI
Brain microstructure
Diffusion MRI

ABSTRACT

$^{23}$Na provides the second strongest MR-observable signal in biological tissue and exhibits bi-exponential $T_2^*$ relaxation in micro-environments such as the brain. There is significant interest in developing $^{23}$Na biomarkers for neurological diseases that are associated with sodium channel dysfunction such as multiple sclerosis and epilepsy. We have previously reported methods for acquisition of multi-echo sodium MRI and continuous distribution modelling of sodium relaxation properties as surrogate markers of brain microstructure. This study aimed to compare $^{23}$Na $T_2^*$ relaxation times to more established measures of tissue microstructure derived from advanced diffusion MRI at 7 T. Six healthy volunteers were scanned using a 3D multi-echo radial ultra-short TE sequence using a dual-tuned $^1$H/$^{23}$Na birdcage coil, and a high-resolution multi-shell, high angular resolution diffusion imaging sequence using a 32-channel $^1$H receive coil. $^{23}$Na $T_2^*$ relaxation parameters [mean $T_2^*$ ($T_{2mean}^*$) and fast relaxation fraction ($T_{2ff}^*$)] were calculated from a voxel-wise continuous gamma distribution signal model. White matter (restricted anisotropic diffusion) and grey matter (restricted isotropic diffusion) density were calculated from multi-shell multi-tissue constrained spherical deconvolution. Sodium parameters were compared with white and grey matter diffusion properties. Sodium $T_{2mean}^*$ and $T_{2ff}^*$ showed little variation across a range of white matter axonal fibre and grey matter densities. We conclude that sodium $T_2^*$ relaxation parameters are not greatly influenced by relative differences in intra- and extracellular partial volumes. We suggest that care be taken when interpreting sodium relaxation changes in terms of tissue microstructure in healthy tissue.

## 1. Introduction

Sodium is the second strongest MR-observable nucleus in biological tissue. In the brain, sodium ions are involved in the maintenance of osmolality and in the generation of ionic gradients that are the source of membrane potentials. Changes in sodium levels can therefore be a marker for cellular pathophysiology.

Sodium nuclei have spin 3/2 with 4 states (3/2, 1/2, −1/2, −3/2). In fast motion regimes such as cerebrospinal fluid, local electric field gradients cancel out and all transitions between spin states occur at the same rate resulting in mono-exponential $T_2^*$ decay. In slower motion regimes such as brain tissue, the splitting of energy levels is shifted due to the non-vanishing local electric field gradients resulting in faster satellite transitions between 3/2 to 1/2 states compared to the slower central spin transitions. This manifests as bi-exponential $T_2^*$ decay when measured during an MRI experiment. The ratio of satellite and central spin transitions is 3:2 respectively, however, local motion regimes within an imaging voxel lead to a continuum of fast and slow $T_2^*$ decay times (Syeda et al., 2019).

Identifying and measuring the relative MRI signal contributions of satellite and central transitions has become a major focus of sodium MRI research. Several strategies have emerged including: triple quantum filtering (Fleysher et al., 2013; Griffey et al., 1990; Hancu et al., 1999; Tsang et al., 2012; Worthoff et al., 2019) to filter signals attributable to

* Corresponding author. Department of Neuroscience, Central Clinical School, Monash University, 99 Commercial Road, Prahran, Victoria, 3181, Australia.
*E-mail address:* scott.kolbe@monash.edu (S.C. Kolbe).
[1] Authors contributed equally to the manuscript.

https://doi.org/10.1016/j.neuroimage.2020.116609
Received 2 September 2019; Received in revised form 30 January 2020; Accepted 4 February 2020
Available online 7 February 2020

triple quantum coherences, inversion recovery sequences (Stobbe and Beaulieu, 2005) to annul signals with long T1 such as cerebro-spinal fluid, and quantitative $T_2^*$ mapping using multi-echo sequences to characterise the relative $T_2^*$ times of fast and slow decaying signals (Blunck et al., 2017; Riemer et al., 2018).

Our own work has focussed on quantitative $T_2^*$ mapping as it allows for reasonable imaging resolution (3.1 mm isotropic) and SNR at 7T. We have reported fast and slow $^{23}$Na $T_2^*$ decay times using a novel 3D multi-echo radial sequence (3D-MERINA) (Blunck et al., 2017). More recently, we extended the signal characterisation applied to multi-echo sodium MRI data to allow for continuous distribution modelling of $T_2^*$ using the gamma distribution to obtain two useful and robust parameters that can potentially act as surrogates for changes in sodium in brain tissue: mean $T_2^*$ decay time ($T_{2mean}^*$) and the fraction of fast $T_2^*$ decay ($T_{2ff}^*$) (Syeda et al., 2019). These parameters were able to differentiate different agarose concentrations *in-vitro* with greater sensitivity than a bi-exponential model, and showed sensible differences in distributions between brain tissue and cerebrospinal fluid *in-vivo*.

Several recent studies have suggested that relaxation of satellite transitions during sodium imaging might provide information regarding intracellular volume fractions in tissue and as such, sodium imaging might provide markers for axonal density and metabolic dysfunction (Fleysher et al., 2013; Petracca et al., 2016; Worthoff et al., 2019). This study aimed to further explore sources of variance in $^{23}$Na $T_{2mean}^*$ and $T_{2ff}^*$ in the human brain *in-vivo* by comparing these parameters with tissue microstructural features obtained from advanced diffusion MRI at 7 T. In this study we used a high-resolution multi-shell diffusion acquisition together with a spherical deconvolution based diffusion modelling technique (Jeurissen et al., 2014) to provide surrogate markers of intra-axonal and intra-cellular volume fractions. At high diffusion weighting (e.g. $b = 3000$ s/mm$^2$ as was used in this study), signal from fast diffusing water molecules is assumed to be attenuated such that only signal from intra-cellular molecules experiencing restricted diffusion remains. Thus, the axonal fibre density or grey matter densities are considered to be proportional to the intra-cellular volume fractions (Raffelt et al., 2012).

The motivation for the study was to test the hypothesis that sodium relaxation distributions are affected by the intracellular volume fraction that can be measured using diffusion MRI and advanced image processing techniques that can provide markers for axonal and grey matter densities. Specifically, we hypothesised that shorter $T_{2mean}^*$ and higher $T_{2ff}^*$ would be associated with greater density of axons in white matter and grey matter density based on diffusion MRI microstructural measures.

## 2. Methods

### 2.1. MRI acquisition and analysis

Six healthy subjects (age (mean/range) 29/22-39, sex 3f/3m) were imaged using a research 7T MRI scanner (Magnetom, Siemens Healthcare, Erlangen, Germany) with a single channel transmit/receive dual-tuned $^1$H-$^{23}$Na head coil (QED, Mayfield Village, Ohio USA) for sodium imaging and a 32-channel transmit/receive $^1$H head coil (Nova Medical, MA, USA) for anatomical and diffusion imaging.

Acquired MRI sequences included:

1) 3D multi-echo radial UTE sequence (3D-MERINA): TR = 150 ms, 42 echoes with initial echo time = 400 μs, $T_{RO}$ = 1.8 ms, FOV = 20 cm, Cartesian regridded to 3.1 mm isotropic resolution with N = 8,000 projections (scan time = 22 min) (Blunck et al., 2017);
2) MP2RAGE anatomical sequence (TR = 4700 ms, TE = 2.89 ms, TI = 700/2700 ms, matrix size = 256*256, FOV = 256*256 mm$^2$, slice thickness = 1 mm, scan time = 6 min); and
3) Multi-shell diffusion weighted sequence (103 diffusion directionally encoded scans distributed across four shells $b = 0/1000/2000/3000$ s/mm$^2$, multiband slice acceleration factor = 3, GRAPPA phase acceleration factor = 2, 1.25 mm isotropic resolution, phase-encoding anterior-posterior, scan time = 13 min). Sequence parameters were based on published optimised values (Vu et al., 2015). A separate non-diffusion encoded image was acquired with reverse phase-encoding direction to calculate a field-map for magnetic susceptibility distortion correction.

This study was approved by the University of Melbourne Human Research Ethics Committee and all subjects provided written voluntary consent to participate in the study. An anonymised copy of raw imaging data and analysis code included in this manuscript can be made available upon request to the corresponding author.

### 2.2. Sodium decay model

$T_2^*$ sodium decay was modelled using a continuous gamma distribution model as previously described (Syeda et al., 2019). Briefly, the measured signal $M$ as a function of echo time $t$ is given by:

$$M(t,\ R_2^*) = M_0 \int e^{-t/R_2^*} p(R_2^*)\ dR_2^*, \quad [1]$$

where the relaxation rate $R_2^*$ is modelled as a gamma probability distribution with shape ($k$) and scale ($\theta$) parameters:

$$p(R_2^*, k, \theta) = \frac{1}{\theta^k \Gamma(k)} R_2^{*k-1} e^{-R2^*/\theta}. \quad [2]$$

This leads to the signal model:

$$M(t; M_0,\ k,\ \theta) = M_0(1+\theta t)^{-k}. \quad [3]$$

Parameters ($M_0$, $k$, $\theta$) were estimated for each voxel independently using sodium magnitude images. Sodium MRI data has relatively poor signal to noise ratio, especially for later echoes. Maximum Likelihood (ML) parameter estimation was carried out via a Rician distributed log-likelihood function, where the Rayleigh noise variance, $\sigma^2$, was estimated from a region of interest in the image background. ML parameter estimation was performed in MATLAB using a constrained multivariate solver initialised with $R_2^* = 150$ ms$^{-1}$ to ensure convergence on biologically plausible values for $R_2^*$.

We defined two parameters of interest $T_{2mean}^*$ and $T_{2ff}^*$ from the fitted $k$ and $\theta$ parameters:

$$T_{2\ mean}^* = {}^1/_{k\theta}, \quad [4]$$

and

$$T_{2\ ff}^* = \int_0^{T_{2\ thresh}^*} p(T_2^*) \mathrm{d}T_2^*. \quad [5]$$

$T_{2mean}^*$, the reciprocal of the mean of the gamma distribution fitted to $R_2^*$, can be interpreted as the modelled mean $T_2^*$ of an individual voxel. $T_{2ff}^*$ is the proportion of the distribution that lies below a threshold $T_2^*$ value. We selected a threshold of 15 ms based on previous reports in the literature (Madelin et al., 2014). Fig. 1 shows example gamma model fits for $T_2^*$ sodium signal decay curves from three representative voxels in white matter, grey matter and CSF respectively.

### 2.3. Image analysis

Fig. 2 provides an overview of the image data acquired and analysed in this study. Raw multi-echo sodium data was reconstructed to 3.125 mm$^3$ isotropic Cartesian voxels according to previously published

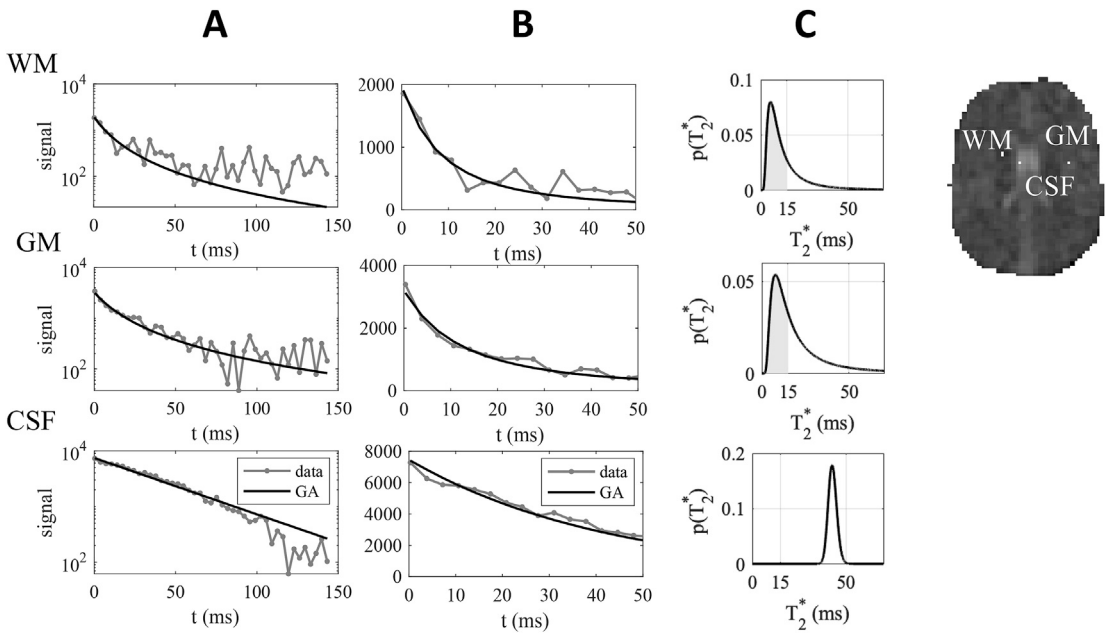


**Fig. 1.** (A) Measured MR signal decay (left column, grey data points) overlayed with fitted curve (black line) for (A) all echoes and (B) for first 50 ms, as well as (C) associated gamma distributions for $T_2^*$ with relative fast fraction shown (filled grey region). Data are shown for three representative voxels taken from white matter (WM), grey matter (GM) and CSF respectively. Note that modelled curve fits (black lines) do not follow the data (grey), due to Rician noise bias in the data that is accounted for in the model.

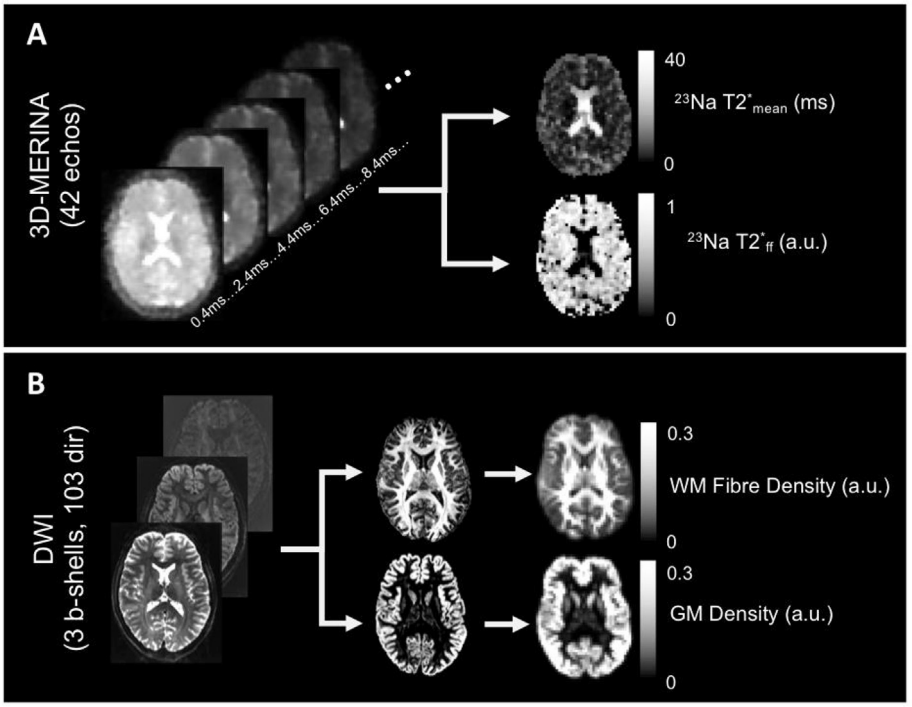


**Fig. 2.** Overview of raw and processed imaging data including (A) 3D-MERINA and associated $T_{2\text{mean}}^*$ and $T_{2\text{ff}}^*$ maps, and (B) multi-shell DWI and associated WM fibre density and grey matter density maps were calculated from high resolution data and coregistered/resampled to the image resolution of the sodium scans.

methods (Blunck et al., 2017). The (denoised) $T_1$-weighted anatomical MP2RAGE image was segmented to identify grey matter, white matter and CSF using FSL-FAST (Zhang et al., 2001). MP2RAGE UNI-DEN images were aligned to sodium MRI data using a two-step procedure. First, the UNI-DEN images were manually aligned to the first echo sodium scan using tkregister2, a tool contained within the Freesurfer MRI analysis toolkit (https://surfer.nmr.mgh.harvard.edu). After manual alignment, affine registration (FSL, FLIRT) (Jenkinson et al., 2002) was used to fine-tune the registration. Additionally, the UNI-DEN image was registered to standard MNI space using FLIRT. Grey matter (MNI atlas) and white matter (JHU tractography atlas) regions of interest contained within the FSL package were thresholded (>40%), binarized and registered to sodium MRI data through the concatenation of MNI-to-MP2RAGE and MP2RAGE-to-$^{23}$Na transformation matrices. For

each subject, mean $^{23}$Na $T^*_{2mean}$ and $T^*_{2ff}$ were calculated for whole GM/WM/CSF and regional GM and WM ROIs. Summary statistics were calculated for the group for each ROI.

Raw DWI data was pre-processed to correct for susceptibility and eddy-current induced spatial distortions using FSL TOPUP and EDDY and the B0 image was co-registered to the MP2RAGE data using FLIRT (Jenkinson et al., 2002) and transformations from DWI space to sodium MRI space were calculated from the DWI-to-MP2RAGE and MP2RAGE--to-$^{23}$Na transformation matrices. Corrected DWI data were then processed using multi-shell multi-tissue constrained spherical deconvolution (MSMT-CSD) (Jeurissen et al., 2014) in MRtrix 3.0 to obtain maps of WM fibre density, GM density and CSF density according to the methods proposed by Raffelt et al. (2012). Briefly, an automated method was used to identify single fibre WM voxels, pure GM and CSF voxels and from these, a multi-shell DWI response function was calculated. The response functions were deconvolved from the DWI signal to produce fibre orientation distribution functions, the volume integral of which was taken to be the "density" of WM/GM/CSF. To minimise the inclusion of voxels containing high partial volume of CSF, all voxels with CSF partial volume (calculated from MP2RAGE segmentation) over 10% were excluded from further analyses. Voxelwise comparisons were performed between $^{23}$Na $T^*_{2mean}$ and $T^*_{2ff}$ and WM and GM density maps in pure WM

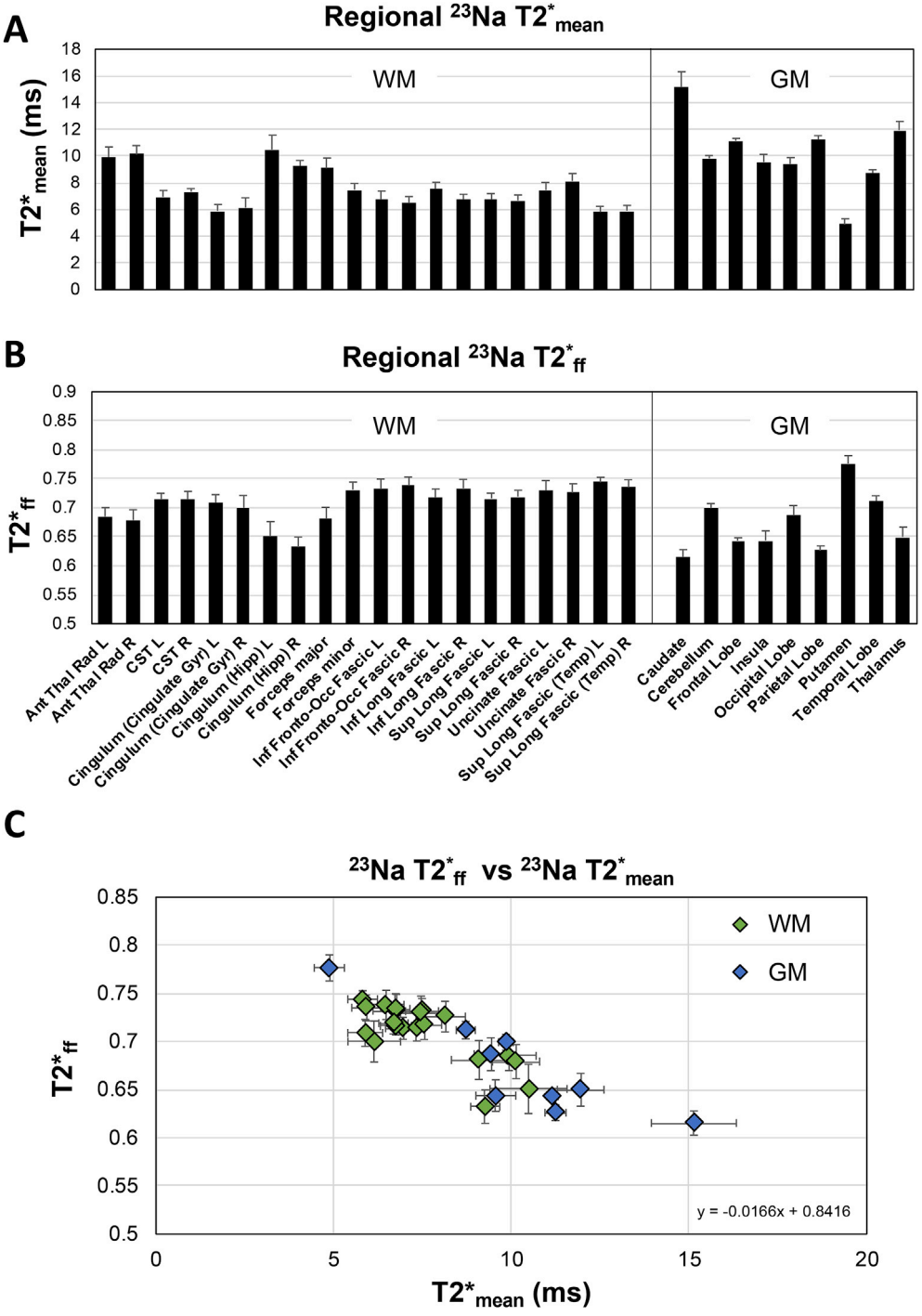


**Fig. 3.** Shows mean (A) $^{23}$Na $T^*_{2mean}$ and (B) $T^*_{2ff}$ values across subjects for white and grey matter regions of interest. (C) Regional $T^*_{2mean}$ and $T^*_{2ff}$ were strongly

and GM voxels, and between $^{23}$Na $T^*_{2mean}$ and $T^*_{2ff}$ and partial volume inclusion of WM and GM as determined by MP2RAGE segmentation.

### 2.4. Statistical analyses

Summary statistics were computed for regional $^{23}$Na $T^*_{2mean}$ and $T^*_{2ff}$ from grey and white matter regions of interest to study variation in these parameters across the brain. For all subjects, $^{23}$Na parameters were compared voxelwise with axonal fibre and grey matter densities measured from multi-shell diffusion weighted imaging using linear regression models. All statistical analyses were performed using MATLAB 2018a.

## 3. Results

### 3.1. Regional $^{23}$Na $T^*_2$ in grey and white matter

Variation was observed in $^{23}$Na $T^*_{2mean}$ (Fig. 3A) and $T^*_{2ff}$ (Fig. 3B) across white matter pathways and grey matter regions. In white matter, the left [mean (SD) $T^*_{2mean} = 9.92$ (0.76) ms; $T^*_{2ff} = 0.69$ (0.02)] and right [$T^*_{2mean} = 10.13$ (0.66) ms; $T^*_{2ff} = 0.68$ (0.02)] anterior thalamic radiations and the left [$T^*_{2mean} = 10.48$ (1.08) ms; $T^*_{2ff} = 0.65$ (0.03)] and right [$T^*_{2mean} = 9.26$ (0.40) ms; $T^*_{2ff} = 0.63$ (0.02)] hippocampal cingulum bundles had the highest $^{23}$Na $T^*_{2mean}$ and the lowest $T^*_{2ff}$ respectively. $^{23}$Na $T^*_{2mean}$ and $T^*_{2ff}$ were fairly consistent across the remainder of the white matter ($T^*_{2mean} = 5$–9 ms; $T^*_{2ff} = 0.67$–0.73).

Greater variation was seen in grey matter $^{23}$Na. The caudate had the highest $T^*_{2mean}$ [15.13 (1.20) ms] and the lowest $T^*_{2ff}$ [0.61 (0.01)], and the putamen had the lowest $T^*_{2mean}$ [4.88 (0.42) ms] and the highest $T_2{}^*_{ff}$ [0.77 (0.01)]. $^{23}$Na $T^*_{2mean}$ was significantly negatively correlated with $T^*_{2ff}$ across WM and GM regions of interest ($R = -0.87$, $p < 0.0001$; $T^*_{2ff} = -0.017 * T^*_{2mean} + 0.84$) (Fig. 3C).

### 3.2. Correlation between $^{23}$Na T2* and WM/GM microstructure

Fig. 4 shows results from a single example subject for voxel-wise 2D histogram comparisons between $^{23}$Na ($T^*_{2ff}$ and $T^*_{2mean}$) and diffusion (WM fibre density and GM density) MRI parameters. In white matter, neither $T^*_{2ff}$ nor $T^*_{2mean}$ were strongly correlated with WM fibre density. $T^*_{2ff}$ consistently ranged between 0.6 and 0.8 across a wide range of fibre densities (Fig. 4A). Although variability in $T^*_{2mean}$ decreased for higher WM fibre density values, there was no clear linear trend (Fig. 4B). In grey matter, there did appear to be weak correlations between higher GM density and lower $T^*_{2ff}$ and higher $T^*_{2mean}$, although there was considerable spread in the data (Fig. 4C/D).

Across all subjects, regression slopes for these comparisons were highly consistent (Table 1). In white matter, a single unit change in WM fibre density was associated with a mean (SD) of 0.10 (0.06) units change in $T^*_{2ff}$ and −8.83 (2.24) ms change in $T^*_{2mean}$. In grey matter, a single unit change in GM density was associated with a −0.03 (0.03) units change in $T^*_{2ff}$ and 7.12 (1.64) ms change in $T^*_{2mean}$.

Due to the low resolution of sodium MRI we also considered the effects of partial volume inclusion of grey and white matter on $^{23}$Na parameters. Again, we noted a consistent $T^*_{2ff}$ (Fig. 5A) and $T^*_{2mean}$ (Fig. 5B) across a range of GM/WM partial volumes (calculated by MP2RAGE segmentation). For these comparisons, regression slopes were highly consistent across subjects (Table 2) with a 1% change in partial volume predicting a 0.02 (0.004) units change in $T^*_{2ff}$ and a −1.30 (0.14) ms change in $T^*_{2mean}$.

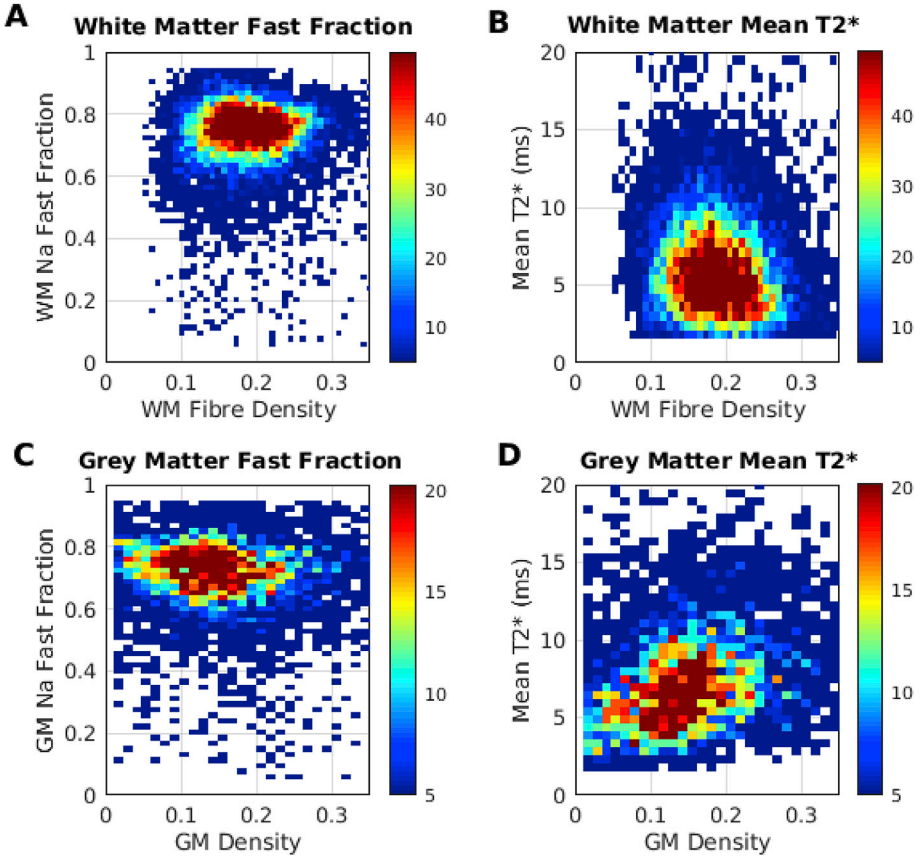


**Fig. 4.** 2D Histograms for voxel-wise comparisons of $^{23}$Na and DWI parameters in a single example subject for voxels containing pure white (A/B) and grey (C/D) matter.

**Table 1**
Shows mean signal and regression slopes (raw and normalised) for comparisons between $^{23}$Na parameters and WM fibre density and GM densities derived from multi-shell diffusion MRI.

| Subject | Voxels Tested | Mean | | Slope | | Slope (normalised) | |
|---|---|---|---|---|---|---|---|
| | | $T^*_{2ff}$ | $T^*_{2mean}$ | $T^*_{2ff}$ | $T^*_{2mean}$ | $T^*_{2ff}$ | $T^*_{2mean}$ |
| 01 | WM | 0.735 | 6.225 | 0.057 | −7.162 | 0.030 | −0.122 |
| | GM | 0.703 | 7.670 | −0.054 | 8.691 | −0.038 | 0.223 |
| 02 | WM | 0.718 | 6.326 | 0.137 | −11.480 | 0.058 | −0.161 |
| | GM | 0.697 | 7.613 | −0.036 | 6.294 | −0.018 | 0.117 |
| 03 | WM | 0.710 | 6.500 | 0.093 | −8.556 | 0.038 | −0.117 |
| | GM | 0.689 | 7.679 | −0.003 | 4.895 | −0.001 | 0.090 |
| 04 | WM | 0.787 | 4.264 | 0.145 | −5.624 | 0.096 | −0.120 |
| | GM | 0.761 | 5.310 | −0.046 | 6.695 | −0.043 | 0.210 |
| 05 | WM | 0.760 | 4.838 | 0.175 | −11.058 | 0.093 | −0.188 |
| | GM | 0.731 | 6.166 | 0.005 | 6.787 | 0.003 | 0.135 |
| 06 | WM | 0.728 | 6.409 | 0.014 | −9.109 | 0.008 | −0.162 |
| | GM | 0.697 | 8.155 | −0.074 | 9.369 | −0.049 | 0.238 |
| Mean | WM | 0.740 | 5.760 | 0.104 | −8.832 | 0.054 | −0.145 |
| | GM | 0.713 | 7.099 | −0.034 | 7.122 | −0.025 | 0.169 |
| SD | WM | 0.029 | 0.959 | 0.060 | 2.245 | 0.036 | 0.029 |
| | GM | 0.028 | 1.106 | 0.031 | 1.640 | 0.022 | 0.062 |

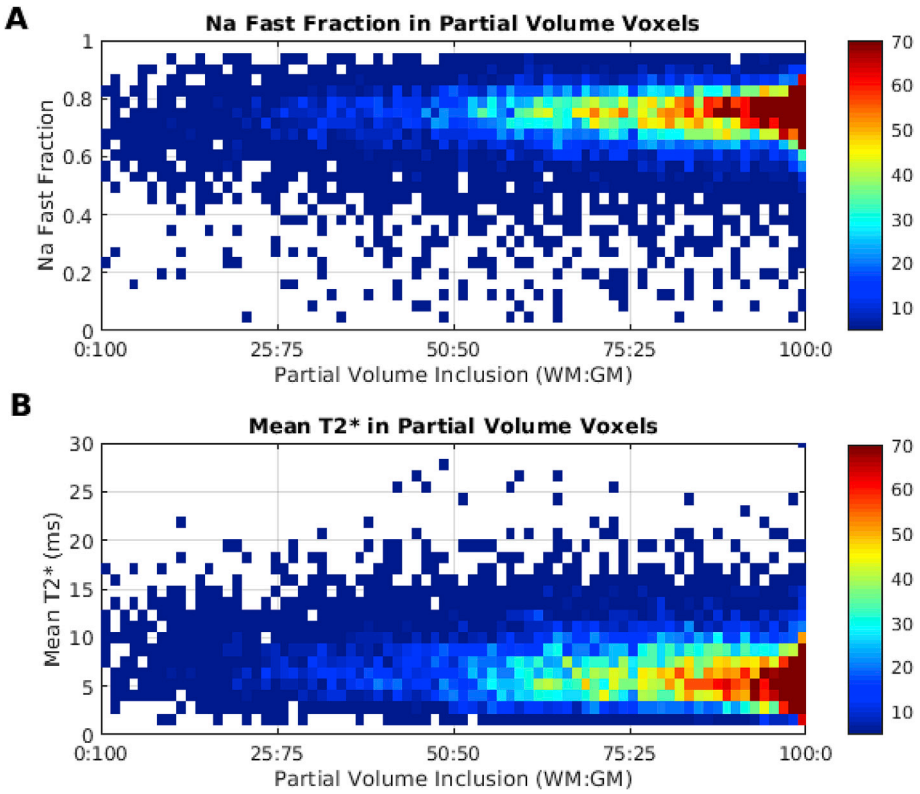


**Fig. 5.** 2D Histograms for voxel-wise comparisons of $^{23}$Na parameters in a single example subject for voxels with varying degrees of partial volume inclusion of grey and white matter calculated from probabilistic segmentation of MP2RAGE anatomical images.

## 4. Discussion

This study aimed to explore the microstructural correlates of two parameters derived from continuous $T^*_2$ distribution modelling of $^{23}$Na MRI ($T^*_{2mean}$ and $T^*_{2ff}$) in healthy human brain white and grey matter *in-vivo* at 7 T. It has previously been stated that differences in tissue microstructure can influence the relative volume fractions of the fast- and slow-relaxing components due to differences in motion regimes that are found between the intra- and extra-cellular environment (Petracca et al., 2016). Based on this reasoning it can be hypothesised that regions of higher axonal or grey matter densities in the brain (higher intra-cellular volume fractions) will be associated with faster $^{23}$Na $T^*_2$ relaxation rates. We tested this hypothesis by comparing $^{23}$Na $T^*_2$ relaxation rates with axonal and grey matter densities measured using multi-shell diffusion weighted imaging.

In contrast to our expectations, we observed relatively consistent $T^*_{2mean}$ and $T^*_{2ff}$ across a range of axonal fibre and grey matter densities. These results suggest that the relationships between sodium relaxation rates and tissue microstructure cannot be simplistically interpreted in relation to axonal and cellular densities. A recent letter to the editor in the journal *Magnetic Resonance in Medicine* by Burstein and Springer (2019) aimed to revisit assumptions regarding sodium MRI that they felt had been neglected by the field in recent years. The authors made special mention of the fact that sodium relaxation time constants cannot be used

**Table 2**
Shows mean signal and regression slopes (raw and normalised) for comparisons between $^{23}$Na parameters and partial volume (GM:WM) calculated from probabilistic segmentation of MP2RAGE anatomical images.

| Subject | Mean | | Slope (raw, $*10^{-1}$) | | Slope (normalised) | |
|---|---|---|---|---|---|---|
| | $T^*_{2ff}$ | $T^*_{2mean}$ | $T^*_{2ff}$ | $T^*_{2mean}$ | $T^*_{2ff}$ | $T^*_{2mean}$ |
| 01 | 0.724 | 6.833 | 0.027 | −1.320 | 0.112 | −0.190 |
| 02 | 0.708 | 6.771 | 0.023 | −1.368 | 0.089 | −0.183 |
| 03 | 0.704 | 6.799 | 0.021 | −1.185 | 0.082 | −0.161 |
| 04 | 0.777 | 4.647 | 0.017 | −1.136 | 0.099 | −0.212 |
| 05 | 0.747 | 5.245 | 0.018 | −1.255 | 0.078 | −0.183 |
| 06 | 0.718 | 7.115 | 0.024 | −1.518 | 0.128 | −0.280 |
| Mean | 0.730 | 6.235 | 0.022 | −1.297 | 0.098 | −0.201 |
| SD | 0.028 | 1.024 | 0.004 | 0.138 | 0.019 | 0.042 |

to differentiate intra- and extracellular sodium signals due to the complexity of the extracellular environment and labile macromolecular interactions producing a small $T_2^*$ values in both the intra- and extra-cellular environments. Our findings of relatively poor correlations between $^{23}$Na parameters and white and grey matter densities support these interpretations. Diffusion MRI is generally considered to be the most promising method for characterising neural tissue microstructure, however it is important to recognise that all diffusion analysis methods that attempt to identify fibre Orientation Distribution Functions contain assumptions that are difficult to verify experimentally. In the case of constrained spherical deconvolution, the tissue response functions are calculated from "pure" voxels of single fibre WM, GM and CSF and then assumed to be correct for all voxels throughout the data set. However, variation in cell sizes, densities, permeabilities and packing configurations are likely to contribute to ill-fitting of the response functions that leads to variance in the resultant WM, GM and CSF "densities".

We noted some variability in sodium relaxation parameters across different white and grey matter regions. In white matter, mean $T_2^*$ was consistently between 6 and 8 ms across most regions except the anterior thalamic radiations, the hippocampal cingulum bundles and the forceps major where mean $T_2^*$ was closer to 10 ms. In grey matter, mean sodium $T_2^*$ was greatest in the caudate and lowest in the neighbouring putamen. These results are, to a degree, consistent with those reported by Ridley and colleagues (Ridley et al., 2018) who noted a larger proportion of long $T_2^*$ in the caudate compared to the putamen using a bi-exponential fitting procedure to multi-echo data. While care was taken to avoid partial volume inclusion of CSF in masks, even a small partial volume inclusion of CSF in the caudate mask could explain the large increase in mean $T_2^*$ in that region in our data. In contrast, one might expect an influence of tissue susceptibility on sodium relaxation constants, the putamen is a region of relatively high magnetic susceptibility due to the presence of iron which could explain the shorter relaxation constant in that region. A limitation of this study is the lack of $B_0$ and $B_1$ field effects in our relaxation modelling, which should be explored further in future.

Limitations in the acquisition of sodium MRI data that must be considered when interpreting these results. The lower abundancy and rapid relaxation of sodium (especially of satellite transitions) make the signal to noise ratio of sodium imaging relatively low compared to proton imaging, even at higher magnetic fields such as 7T. In order to adequately traverse k-space we used an ultra-short TE sequence with 8000 radial k-space trajectories re-gridded to Cartesian k-space at an image resolution of 3.1 mm isotropic. This resolution is reasonable for a multi-echo sequence for relaxometry. In comparison, triple quantum filtered sodium imaging tends to be acquired with resolution ~10 mm (Petracca et al., 2016; Worthoff et al., 2019). However, the relatively large voxel sizes and long scan time with associated increased risk of subject movement, make partial volume inclusion of adjacent tissue types at boundaries a potential problem. Given the large contribution to the sodium signal from CSF, we excluded voxels with >10% CSF signal contribution (as determined by MP2RAGE segmentation) and specifically studied the effect of partial volume inclusion of WM and GM on sodium relaxation parameters. Interestingly we found very little variation in sodium relaxation was explained by partial volume inclusion of GM and WM, suggesting that sodium relaxation is somewhat agnostic to the microstructural alignment of tissue microstructure. However, given the image resolution and the thickness of the cortical sheet, identifying GM voxels in the cortex that are devoid of CSF partial volume inclusion is challenging. Future studies could investigate a combination of inversion recovery during acquisition to annul CSF signal and multi-echo fitting to identify variations in relaxation.

## 5. Conclusions

This is the first study to explore relationships between sodium relaxation constants and brain tissue microstructure. Contrary to theories attributing faster sodium relaxation with greater proportion of intracellular volume, we found that sodium relaxation was consistent across a wide range of white matter axonal fibre and grey matter densities in healthy tissue. We suggest that care be taken when interpreting sodium relaxation in terms of intra- and extra-cellular volumes.

## CRediT author statement

**Scott C. Kolbe:** Conceptualization, Methodology, Software, Formal analysis, Investigation, Resources, Data Curation, Writing - Original Draft, Writing - Review & Editing, Visualization, Project administration, Funding acquisition.

**Warda Syeda:** Conceptualization, Methodology, Software, Formal analysis, Writing - Review & Editing, Visualization.

**Yasmin Blunck:** Conceptualization, Methodology, Software, Formal analysis, Investigation, Resources, Writing - Review & Editing, Visualization.

**Rebecca Glarin:** Conceptualization, Methodology, Investigation, Resources, Data Curation, Writing - Review & Editing, Project administration.

**Meng Law:** Writing - Review & Editing, Supervision, Funding acquisition.

**Leigh Johnston:** Conceptualization, Methodology, Writing - Review & Editing, Supervision.

**Jon O. Cleary:** Conceptualization, Methodology, Software, Investigation, Resources, Data Curation, Writing - Review & Editing, Project administration, Supervision.

## Declaration of competing interest

The authors report no conflicts of interest relating to this work.

## Acknowledgements

This work was supported by Melbourne Neuroscience Institute, University of Melbourne. We acknowledge the facilities, and the scientific and technical assistance of the Australian National Imaging Facility at the Melbourne Brain Centre Imaging Unit. The Australian National Imaging Facility is funded by the Australian Government NCRIS program. The work was also supported by a research collaboration agreement with Siemens Healthineers. The MP2RAGE data was acquired with a "Works in Progress" prototype sequence provided by Siemens Healthineers. JOC was supported by a University of Melbourne McKenzie Fellowship.

## Appendix A. Supplementary data

Supplementary data to this article can be found online at https://doi.org/10.1016/j.neuroimage.2020.116609.

## References


Blunck, Y., Josan, S., Taqdees, S.W., Moffat, B.A., Ordidge, R.J., Cleary, J.O., Johnston, L.A., 2017. 3D-multi-echo radial imaging of 23 Na (3D-MERINA) for time-efficient multi-parameter tissue compartment mapping. Magn. Reson. Med. 79, 1950–1961.

Burstein, D., Springer Jr., C.S., 2019. Sodium MRI revisited. Magn. Reson. Med. 82, 521–524.

Fleysher, L., Oesingmann, N., Brown, R., Sodickson, D.K., Wiggins, G.C., Inglese, M., 2013. Noninvasive quantification of intracellular sodium in human brain using ultrahigh-field MRI. NMR Biomed. 26, 9–19.

Griffey, R.H., Griffey, B.V., Matwiyoff, N.A., 1990. Triple-quantum-coherence-filtered imaging of sodium ions in vivo at 4.7 tesla. Magn. Reson. Med. 13, 305–313.

Hancu, I., Boada, F.E., Shen, G.X., 1999. Three-dimensional triple-quantum-filtered (23) Na imaging of in vivo human brain. Magn. Reson. Med. 42, 1146–1154.

Jenkinson, M., Bannister, P., Brady, M., Smith, S., 2002. Improved optimization for the robust and accurate linear registration and motion correction of brain images. Neuroimage 17, 825–841.

Jeurissen, B., Tournier, J.D., Dhollander, T., Connelly, A., Sijbers, J., 2014. Multi-tissue constrained spherical deconvolution for improved analysis of multi-shell diffusion MRI data. Neuroimage 103, 411–426.

Madelin, G., Lee, J.S., Regatte, R.R., Jerschow, A., 2014. Sodium MRI: methods and applications. Prog. Nucl. Magn. Reson. Spectrosc. 79, 14–47.

Petracca, M., Vancea, R.O., Fleysher, L., Jonkman, L.E., Oesingmann, N., Inglese, M., 2016. Brain intra- and extracellular sodium concentration in multiple sclerosis: a 7 T MRI study. Brain 139, 795–806.

Raffelt, D., Tournier, J.D., Rose, S., Ridgway, G.R., Henderson, R., Crozier, S., Salvado, O., Connelly, A., 2012. Apparent Fibre Density: a novel measure for the analysis of diffusion-weighted magnetic resonance images. Neuroimage 59, 3976–3994.

Ridley, B., Nagel, A.M., Bydder, M., Maarouf, A., Stellmann, J.P., Gherib, S., Verneuil, J., Viout, P., Guye, M., Ranjeva, J.P., Zaaraoui, W., 2018. Distribution of brain sodium long and short relaxation times and concentrations: a multi-echo ultra-high field (23) Na MRI study. Sci. Rep. 8, 4357.

Riemer, F., Solanky, B.S., Wheeler-Kingshott, C.A.M., Golay, X., 2018. Bi-exponential (23) Na T2 * component analysis in the human brain. NMR Biomed. 31, e3899.

Stobbe, R., Beaulieu, C., 2005. In vivo sodium magnetic resonance imaging of the human brain using soft inversion recovery fluid attenuation. Magn. Reson. Med. 54, 1305–1310.

Syeda, W., Blunck, Y., Kolbe, S., Cleary, J.O., Johnston, L.A., 2019. A continuum of T2* components: flexible fast fraction mapping in sodium MRI. Magn. Reson. Med. 81, 3854–3864.

Tsang, A., Stobbe, R.W., Beaulieu, C., 2012. Triple-quantum-filtered sodium imaging of the human brain at 4.7 T. Magn. Reson. Med. 67, 1633–1643.

Vu, A.T., Auerbach, E., Lenglet, C., Moeller, S., Sotiropoulos, S.N., Jbabdi, S., Andersson, J., Yacoub, E., Ugurbil, K., 2015. High resolution whole brain diffusion imaging at 7T for the Human Connectome Project. Neuroimage 122, 318–331.

Worthoff, W.A., Shymanskaya, A., Shah, N.J., 2019. Relaxometry and quantification in simultaneously acquired single and triple quantum filtered sodium MRI. Magn. Reson. Med. 81, 303–315.

Zhang, Y., B, M., Smith, S., 2001. Segmentation of brain MR images through a hidden Markov random field model and the expectation-maximization algorithm. IEEE Trans. Med. Imag. 20, 45–57.